

pubs.acs.org/journal/apchd5 Article

# Structural Order and Plasmonic Response of Nanoparticle Monolayers

Allison M. Green, Woo Je Chang, Zachary M. Sherman, Zarko Sakotic, Kihoon Kim, Daniel Wasserman, Delia J. Milliron,\* and Thomas M. Truskett\*



Cite This: ACS Photonics 2024, 11, 1280–1292



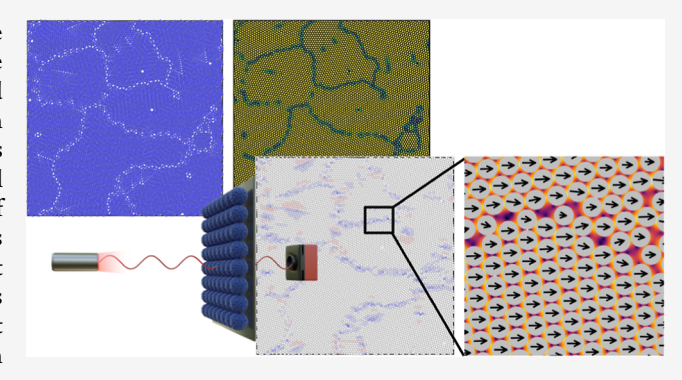
**ACCESS** I

III Metrics & More

Article Recommendations

SI Supporting Information

ABSTRACT: Collective plasmon resonances in superlattice assemblies of metallic nanoparticles are influenced by nanoparticle attributes and assembly structure. Although grain boundaries and other structural defects are inherent to superlattices assembled in the laboratory, their impact on near- and far-field optical properties remains poorly understood. Here, we study variations in structural and optical properties of model two-dimensional superlattices of spherical metallic nanoparticles, focusing on large-scale monolayers of approximately constant area fraction formed by different assembly rates. Our modeling addresses how disorder generates distributions of hot spot intensities and nanoparticle-level resonant frequencies. The highest intensities occur in narrow gaps between particle pairs aligned parallel to field polarization. Despite the



structural diversity of the monolayers investigated, we find the highest hot-spot intensity adjacent to a nanoparticle strongly correlates with the particle's resonant frequency, though the introduction of realistic variability in nanoparticle dielectric parameters weakens the link. These trends hold for different nanoparticle compositions, and predictions are compared with experimentally prepared monolayers of tin-doped indium oxide nanocrystals. Though defectivity only modestly influences ensemble extinction peak frequency and surface-enhanced infrared absorption, increasing structural disorder broadens spectral lineshapes and boosts surface-enhanced Raman scattering enhancement factors. The magnitude of spectroscopic enhancement and the sensitivity of optical properties to local structural order depend primarily on dipole polarizability contrast. These results can help inform tolerances and trade-offs relevant to designing materials and assembly protocols to achieve desired optical properties for applications, including sensitive molecular detection.

KEYWORDS: localized surface plasmon resonance, defect tolerance, near-field enhancement, electromagnetic simulations, superlattice, nanocrystal

# INTRODUCTION

Conduction electrons in metallic nanoparticles interact with light collectively through the localized surface plasmon resonance (LSPR). Absorption and scattering give rise to peaks in extinction spectra at the LSPR frequency, and the electric field intensity is greatly enhanced near each excited nanoparticle. Coupling between LSPR of adjacent nanoparticles produces rich optical phenomena influencing farfield spectra and strengthening the near-field enhancement (NFE). At resonance, closely spaced metal nanoparticles assembled in ordered superlattices create near-field hot spots in their interstitial spaces where the NFE can be several orders of magnitude higher than around isolated nanoparticles. The heightened electric field allows sensitive detection of molecules in the gaps by surface-enhanced Raman scattering (SERS) or surface-enhanced infrared absorption (SEIRA).<sup>1,2</sup>

The spatial arrangement of an assembly's colloidal nanoparticles and its structure-dependent optical properties depend on the assembly protocol. When nanoparticles are allowed sufficient time to diffuse and self-organize, they tend toward structures that minimize free energy. Colloids with isotropic and nonspecific interactions favor highly coordinated superlattices that maximize the density of near-field hot spots, <sup>3,4</sup> and regularly shaped, ligand-capped nanoparticles readily organize into close-packed two-dimensional (2D) and three-dimensional (3D) superlattices. <sup>5-7</sup> Assembly of well-ordered superlattices has advanced with the aid of air—liquid interfaces and immiscible liquid subphases. <sup>7-13</sup> The most regular lattices with minimal defects can be formed by synthesizing nanoparticles

Received: December 9, 2023 Revised: February 6, 2024 Accepted: February 7, 2024 Published: February 22, 2024





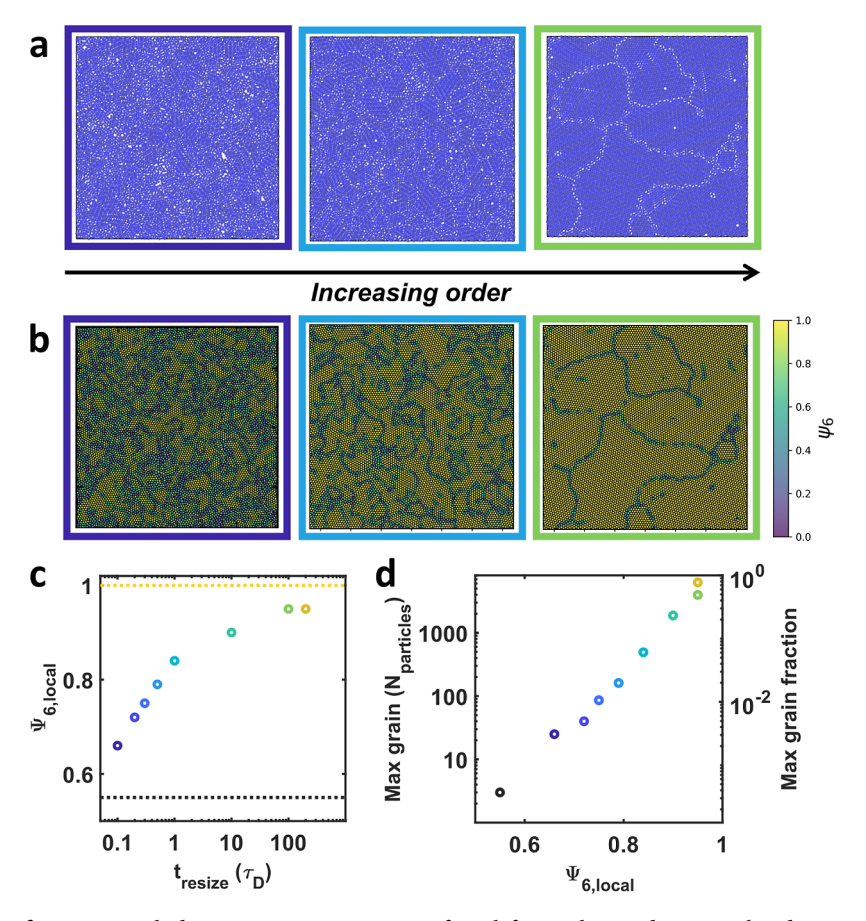


Figure 1. (a) Simulated configurations with decreasing compression rate from left to right. Borders are colored to match the corresponding data points in (c,d). (b) Voronoi diagrams for these configurations with cells colored to indicate each particle's bond-orientational order parameter (see Methods). (c) Average local bond-orientational order parameter for configurations as a function of time  $(t_{resize})$  used to compress from an initial area fraction of 0.2 to  $\approx$ 0.9 in the final state. The orange dotted line represents a perfect lattice; the black dotted line denotes an equilibrated hard-sphere fluid monolayer at its freezing point (i.e., area fraction of 0.66). (d) Maximum grain size as a function of local bond-orientational order. The black circle denotes the same equilibrated fluid as the black dotted line in (c).

with highly uniform size and shape distributions.<sup>3,14</sup> Still, variations among nanoparticles are always present, and low-defectivity assemblies remain challenging to form. All superlattices made in the lab have some disorder.<sup>15</sup>

How optical properties of extended plasmonic assemblies relate to their structure and nanoparticle characteristics remains poorly understood, which poses challenges for designing nanoparticle-based photonic materials. Highly ordered multilayer superlattices of large Au nanoparticles 16,17 support plasmon-polaritons, 18 characterized by a distinctive band structure and bandgap. The spectral features of polaritonic absorption modes have been reported to broaden and disappear altogether with decreasing nanoparticle uniformity or diminishing superlattice quality. 14 However, no specific structure-property relations have been established to fully understand or predict these trends, a point that is underscored by the recent observation that plasmon-polariton resonances can also be supported in structurally disordered multilayers of Au nanoparticles on a mirror with highly uniform interparticle gaps templated by a molecular spacer. 19 Nanoparticle polydispersity or small variations in positional ordering relative to a perfect structure are predicted to increase the variability of electric-field intensity in superlattices.<sup>20</sup> Other implications of structural disorder for the near- and far-field optical properties of plasmonic superlattices 14,16,20,21 and

arrays<sup>22–24</sup> have been demonstrated, but unifying concepts and design principles have proven elusive.

One difficulty has been identifying a practical theoretical framework for computing the optical response of extended plasmonic assemblies with complex structural ordering. Neither mean-field predictions from Maxwell-Garnett theory<sup>2</sup> nor phenomenological plasmon rulers<sup>26-28</sup> consider the type of information that can distinguish assemblies with different types and degrees of structural disorder. Conventional fullwave electrodynamic simulations, e.g., finite element methods or finite difference time domain, can model periodic structures but cannot treat the large systems required to account for structural or compositional defects across length scales. Coupled dipole calculations, pioneered by Schatz and Zou to study collective excitations in plasmonic arrays,<sup>29</sup> have been leveraged to probe the impact of structural perturbations on the optical response of DNA-linked metal nanospheres in finite-sized aggregates<sup>30</sup> and superlattices by considering modest particle-size polydispersity and variable displacements from lattice sites. 20 The T-matrix method, 31 which generalizes the coupled dipole approximation to include multipole responses of nanoparticles, has been applied to model disordered composites of spherical metal inclusions in a dielectric medium.<sup>32</sup> Recent implementations incorporate planar interfaces such as supporting substrates or layered media<sup>33</sup> and accommodate 2D periodic boundary conditions

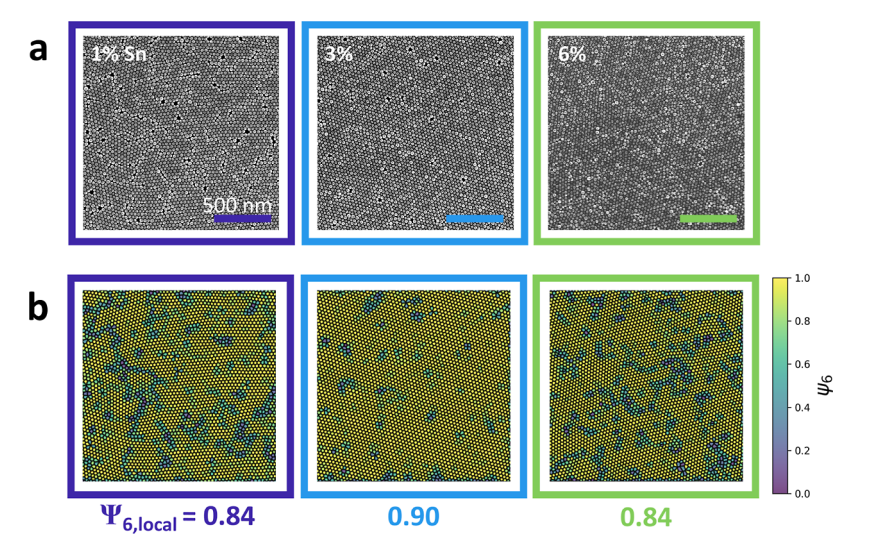


Figure 2. (a) Scanning electron microscopy images of ITO nanocrystal monolayers. (b) Voronoi diagrams of these monolayers, colored to indicate local bond-orientational order. Particle-averaged local bond-orientational order labeled below.

with thousands of particles per simulation cell.<sup>34</sup> In this spirit, we introduced a mutual polarization method (MPM)<sup>35</sup> for efficiently computing the optical response of complex assemblies with 10<sup>4</sup> to 10<sup>5</sup> particles per simulation cell and up to three periodic boundary conditions. This method efficiently solves the many-body mutual polarization problem for dipoles (and quadrupoles) in complex mixtures of spherical particles with different dielectric functions or sizes in any arbitrary spatial arrangement—including particle overlaps and it has been used to successfully predict the experimental optical response of superlattices<sup>35,36</sup> and gel networks<sup>28,35,37</sup>. of plasmonic nanocrystals. Specifically, MPM simulations have shown good agreement with experimentally measured extinction, so reflectance, and effective permittivity of compositionally mixed tin-doped indium oxide nanocrystal monolayers, the extinction of linked tin-doped indium oxide nanocrystal gel networks,<sup>35</sup> and the extinction of gels comprising nanocrystals with mixed size, shape, composition, and ligand length. 28,38 These comparisons with experimental data support MPM's accuracy and utility for studying optical phenomena in complex assemblies. MPM has been further validated with COMSOL finite element method simulations, producing similar results, with small quantitative changes, for predicting the extinction of periodic nanocrystal arrays as well as structure-dependent field intensity trends in random particle arrangements.

Here, we use dipole MPM and Brownian dynamics simulations to predict how structural disorder influences the near- and far-field optical response of monolayers of spherical plasmonic nanoparticles. By simulating a series of monolayers with approximately the same surface coverage but created by progressively faster compressions (analogous to higher solvent evaporation rates in the lab), we model superlattices characterized by an increasing defectivity and structural heterogeneity. We find that with increasing disorder, the distribution of individual nanoparticle resonant frequencies broadens due to variations in local structure. This structural diversity has little effect on the far-field resonance frequency of the ensemble but causes the broadening of the extinction peak and the distribution of near-field intensities. Hot spot intensities near a particle strongly correlate with its local environment, with the highest intensities occurring for the

smallest gaps between particle pairs aligned parallel to the field polarization.

We demonstrate that these trends hold across nanoparticle compositions, with the magnitudes of spectroscopic enhancement factors and sensitivities of the properties to structural disorder being magnified for larger dipole polarizability. For realistic variance in single nanoparticle properties, the distribution of nanoparticle dielectric parameters does not affect the observed disorder-induced enhancement of SERS, although it decreases the SERS enhancement factor by  $\sim\!25\%$  relative to a compositionally uniform monolayer with the same structure. Based on these findings, we suggest possible design strategies for functional plasmonic superlattices with defects.

# ■ RESULTS AND DISCUSSION

**Structural Order.** The structural order present in nanoparticle monolayers is strongly dependent on the assembly protocol. To generate a sequence of structures representative of nanoparticle monolayers assembled in the lab, we used Brownian dynamics simulations to compress 2D-periodic configurations of 8100 spherical particles on a monolayer from an initial area fraction of 0.2 to  $\approx$ 0.9 at different rates (see Methods, Table S1). By varying the compression time over 3 orders of magnitude, from shorter to much longer than the particle diffusion time  $\tau_D$ , final structures with very high to low defectivity levels at approximately the same area fraction were created (Figure 1a,b).

To characterize the structure of the monolayers, we used bond-orientational order and Voronoi tessellation analyses. 6-fold symmetry in the first-neighbor coordination shell can be characterized by the particle-averaged bond-orientational order parameter  $\Psi_{6,local}$ , which attains a value of 0.55 for an equilibrated hard-sphere fluid monolayer at its freezing point (Figures 1c and S1) and approaches unity for a superlattice with perfect hexagonal order. Bond-orientational order analysis is commonly applied in computer simulations and has proven helpful for experimentally characterizing nanoparticle superlattice formation using, e.g., in situ liquid cell transmission electron microscopy and X-ray crosscorrelation analysis. Voronoi tessellation of nanoparticle configurations provides complementary information about the

local structural order. Grains appear as connected clusters of hexagons in the tessellation and grain boundaries present as defect chains of polygons with fewer or more sides than six.<sup>42</sup>

For simulated compression times that are short compared to  $\tau_D$ , particles do not have sufficient time to diffuse and organize into their thermodynamically favored ordered state and instead adopt more disordered nonequilibrium structures <sup>43,44</sup> (Figure 1c). Ordered grains of increasing size, separated by locally disordered grain boundaries, emerge in monolayers prepared by using longer compression times (Figure 1d). Consistent with prior studies, <sup>42</sup> local structural order increases together with the fraction of particles with six neighbors (Figure S2). Slowing the compression rate further to achieve more perfect ordering ultimately faces diminishing returns in Brownian dynamics simulations given the slow cooperative rearrangements required for aligning larger grains.

Experimental monolayers were assembled with tin-doped indium oxide (ITO) nanocrystals using the liquid-air interface method. 8,9,35,36 The nanocrystals were synthesized with varying tin (Sn) dopant concentrations (1, 3, 6%) and had diameters of  $31 \pm 2$  nm (see Methods). The resulting monolayers appear well-ordered but nonetheless show experimental variation (Figure 2a). Using Cellpose, a generalist algorithm for cell segmentation,<sup>45</sup> we conducted the same bond-orientational order and Voronoi tessellation analyses as with the simulated configurations (Figure 2b). This algorithm works well with scanning electron microscopy (SEM) images of nanoparticle assemblies due to their similarity in appearance to cells in culture, having sufficient contrast from their background environment and, therefore, detectable boundaries (Figures S3-S5). Implementations of neural networks, specifically U-Net, to analyze nanoparticle electron microscope data have recently gained interest due to the ability to extract quantitative information from videos and images. 40 The structural order parameters for the experimental monolayers fall within the range of the simulated configurations, validating the appropriateness of our chosen simulation parameters.

**Far-Field Response.** Structural variations in the monolayers affect LSPR coupling and the far-field optical response due to the collective plasmon resonance. To quantify this effect, we adopt the Drude model for the dielectric function of the nanoparticles with parameters mimicking ITO nanocrystals, whose high frequency dielectric constant  $\varepsilon_{\infty}=4\varepsilon_{0}$  (Methods, Table 2). While the compressed Brownian dynamics simulation configurations have an occupied area fraction of  $\approx$ 0.9, this reflects the "thermodynamic" size of each nanoparticle comprising a ligand shell surrounding an optically active inorganic core. We consider the cores to cover a smaller area fraction of 0.73 for our calculations, which corresponds approximately to nanoparticles with a 15 nm radius core surrounded by a 1.7 nm thick ligand shell.

The perfect superlattice's ( $\Psi_{6,local} = 1$ ) extinction peak frequency is remarkably insensitive to the introduction of structural disorder, while the full-width at half-maximum (fwhm) increases for monolayers that are progressively less structured (Figure 3). The insensitivity of the peak frequency is consistent with behavior previously observed in model superlattices where random displacements in lattice sites were introduced to mimic structural imperfections and defects,  $^{20,21}$  though an accompanying peak broadening was not reported in those models. An important difference is that this study considers larger system sizes and an expansive range of heterogeneous superlattice structures produced using different

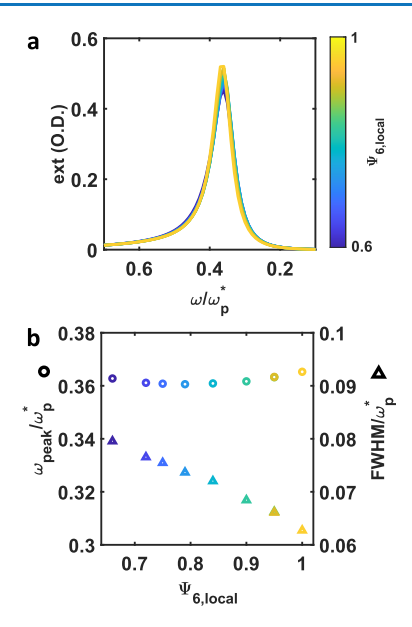


**Figure 3.** (a) Extinction spectra for the series of simulated monolayers in Figure 1 as a function of frequency (nondimensionalized by a modified plasma frequency,  $\omega_{\rm p}^* = \omega_{\rm p}/\sqrt{\varepsilon_{\rm m}}$ ). (b) Normalized resonant peak frequency ( $\omega_{\rm peak}$ , circles) and fwhm (triangles) as a function of the average local bond-orientational order parameter.

assembly rates. Such heterogeneous structures with both amorphous and ordered nanoparticle domains can give rise to peak broadening<sup>21</sup> as well as near-field optical effects we discuss below.

To provide context for the simulations and understand how well our model can inform experiments, we also measured the far-field optical properties (Figure 4, Methods) of the three ITO nanocrystal monolayers, as shown in Figure 2. The extinction measurement taken from a macroscopic area is shown in the main panel of Figure 4a, and we also conducted microscopic measurements using an infrared microscope (inset). After acquiring spectra in the infrared microscope, we captured SEM images of the monolayers from approximately the same areas as the optical measurement for a more direct comparison between structural ordering and optical properties. (Note that the sharp dips and peaks present in both the main panel and inset are due to the vibrational bands of organic ligands. There is noise in the inset spectra due to a lower signal at high frequencies.) Though the structural order present in these samples was not engineered, e.g., by a ratecontrolled assembly process, analyzing the structural and optical response postassembly allows us to compare with our sequence of simulated monolayers and to gain information about the relative sensitivities of the optical response to Sn dopant concentration (1, 3, and 6%) and structural order. The area fractions of the samples were consistent since the nanocrystal size and ligand layer composition (oleate) were kept constant as dopant concentration varied. In previous work, <sup>36</sup> we found an area fraction of 0.73 for similarly prepared monolayers, which is consistent with the simulated area fraction used in this study. The extinction peak frequency varied systematically (Figure S6), having a higher value for greater % Sn as expected, but owing to the consistent packing fraction the peaks lie near the same nondimensional frequency (Figure 4a).33

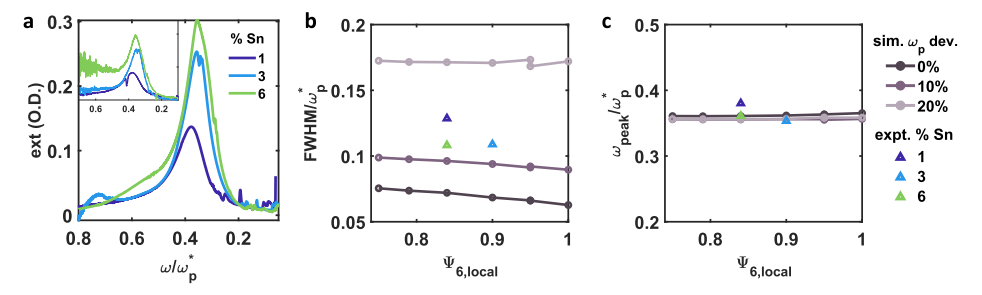


Figure 4. (a) Experimental extinction spectra vs nondimensional frequency  $(\omega/\omega_p^*)$ . Inset: microscopic extinction measured over the same area as SEM images in Figure 2. (b) Extinction fwhm as a function of local bond-orientational order parameter  $(\Psi_{6,local})$  for experiments (triangles) and simulations (circles)—legend on right. Simulations are plotted for the full range of order parameters of Figure 1, assuming normal a distribution of plasma frequencies with different standard deviations. (c) Extinction resonant peak frequency  $(\omega_{peak})$  as a function of  $\Psi_{6,local}$ .

Simulations of our model superlattice monolayers, which assume that each particle has the same dielectric parameters, underestimate the experimental extinction fwhm (Figure 4b). This observation is consistent with previous findings that experimentally prepared nanoparticles are more accurately modeled assuming a distribution of plasma frequencies to capture variations in electron concentration due to nonuniform doping during synthesis<sup>46,47</sup> and variations in particle shape. <sup>48–51</sup> For the ITO nanocrystals studied here, an average experimental electron concentration standard deviation of 12% was extracted from fitting extinction spectra of dilute dispersions using the heterogeneous ensemble Drude approximation (Table S2 and Figure S6a). 46 Plasma frequency varies as the square root of electron concentration; therefore, through error propagation, the expected plasma frequency deviation from this electron concentration spread is approximately 6%. By simulation of configurations with a random normal distribution of plasma frequencies, we observe broader peaks, consistent with this hypothesis. However, the experimental fwhm is marginally broader than the simulations with 10% standard deviation in plasma frequency, indicating that there are additional contributors to experimental spectra broadening beyond nanoparticle electron concentration variation.

While deviations in particle plasma frequency provide one source of disorder, another source of heterogeneity in experimental monolayers is particle size polydispersity. To understand the impact of particle size disorder on the structure and plasmonic response of monolayers, we conducted simulations with a normal distribution of particle diameter with 5, 10, or 20% standard deviation. Similar to the case of monodisperse particles, local bond orientational order increases with decreasing simulation compression rate, but ordering proceeds more slowly for polydisperse particles, and sufficient polydispersity can prevent ordering altogether (Figure S7 and Tables S3, S4). For monolayers with 20% size polydispersity, the local bond orientational order only modestly exceeds that of an equilibrated hard-sphere fluid monolayer, consistent with previous studies which report that highly uniform particle size is critical to the formation of wellordered superlattices. 10,52 We chose to simulate the optical response of the 5 and 10% size polydispersity monolayers, enabling a more direct comparison to the experimental monolayers studied here, which have an average size polydispersity of 7%. When monolayers with different diameter-size distributions over this experimentally relevant range—but the same amount of structural order—are compared, we observe negligible differences in the spectral broadening (Figure S8a).

From SEM image analysis, we calculated an average particle circularity of  $0.92 \pm 0.03$  by comparing the ratio of the area of the particle to the area of a circle with the same perimeter as the particle. A perfect circle has a circularity of 1, and a square has a circularity of 0.77, so the particles studied exhibit significant deviations from spherical shape. Although any influence of shape variation on the resonant frequency of each particle is already approximately accounted for by fitting the ensemble spectra of dispersed nanocrystals with the HEDA model, faceting is expected to allow denser local packing and stronger LSPR coupling. In this way, shape variations could contribute an additional source of heterogeneous broadening to the ensemble resonance spectra of the monolayers.

In contrast to the effect on fwhm, increasing the deviation of nanoparticle plasma frequencies does not have a significant impact on the ensemble peak locations (Figure 4c); the latter are relatively insensitive to disorder in general (Figure 3b). Similarly, particle diameter polydispersity does not significantly impact peak position (Figure S8b). Experiments and simulations agree and collapse to approximately the same superlattice peak frequency. The 1% Sn monolayer is slightly blue-shifted from the other experiments and simulations. This blueshift may be attributed to surface depletion layers that decrease plasmonic coupling and more strongly impact low-doped nanocrystals. <sup>54</sup>

Our simulated and experimental results indicate that, for ITO nanocrystals, variations in the material dielectric function among the ensemble have a stronger impact on the optical properties of superlattices than does structural order. This sensitivity highlights the essential role that synthesizing nanoparticle building blocks with desired (and uniform) properties<sup>14,15,55,56</sup> plays in determining the optical response of monolayer assemblies. The tolerance of these assemblies to structural disorder should have practical implications since relaxing the stringent demand for order allows a wider variety of assembly protocols to be considered for fabrication of monolayers with targeted optical properties.

**Near-Field Response.** While the collective plasmon resonance frequency of superlattice monolayers is insensitive to disorder, the fwhm shows significant broadening due to assembly disorder, and MPM enables us to assess the impact of defects at the nanoparticle scale. Specifically, the extinction spectrum can be decomposed into a sum of contributions from each nanoparticle. The particle-level spectrum is itself a collective property that reflects the spatial organization and optical properties of the surrounding nanoparticles. The distribution of single-particle peak frequencies is sensitive to

configurational disorder (Figure 5a). For the most disordered simulated monolayer ( $\Psi_{6,local} = 0.66$ ), the nanoparticle peak

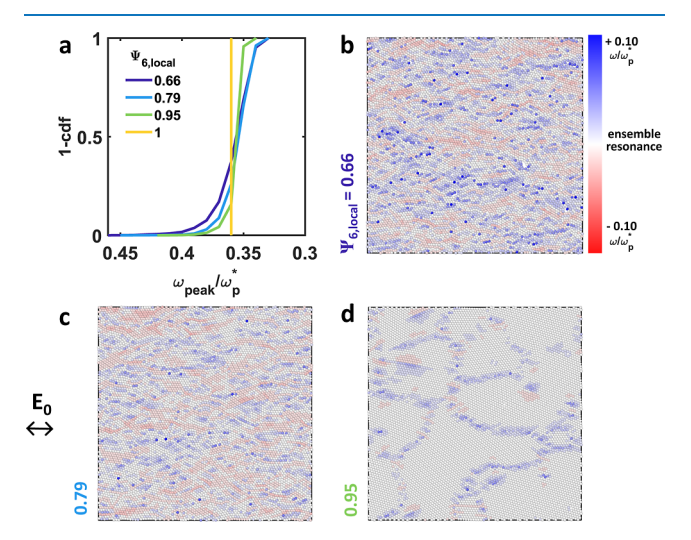


Figure 5. (a) Cumulative distribution function of individual particle resonant frequencies ( $\omega_{\rm peak}$ ) for monolayers with varying average local bond-orientational order. (b–d) Simulated configurations, color-coded by individual particle resonant frequency (blue-shifted or redshifted from the configuration's peak resonant frequency). Average local bond-orientational order parameter  $\Psi_{6,\rm local}$ : (b) 0.66, (c) 0.79, and (d) 0.95. Applied field polarization is indicated by the arrow.

frequency distribution maximally is broadened, and the distribution narrows for monolayers with progressively higher bond-orientational order. In a perfectly ordered superlattice where each particle has an identical environment, there is no spread in nanoparticle peak frequency.

By visualizing the relative peak frequencies in color-coded configurations (Figure 5b-d), we can begin to understand how the structure relates to particle-level shifts. Clusters of particles with red-shifted peaks preferentially align parallel to the electric field polarization, reminiscent of the behavior of one-dimensional chains of closely spaced plasmonic nanoparticles. In highly ordered monolayers (Figure 5d), particles with red- and blue-shifted peaks are located at the grain boundaries, indicating a coupling between the local defect structure and particle-level resonant frequency. Particles in grains with strong 6-fold, bond-orientational order resonate with the ensemble peak frequency.

The distribution of particle-level peak frequencies due to structural disorder in a configuration also relates to the dipole moments induced at a given excitation frequency and the spatial distribution of NFE. For any excitation frequency, some particles will be on- or near-resonance, but others will be offresonance because the structural variations shift their peak frequency. This heterogeneity is evident in near-field intensity maps overlaid with induced nanoparticle imaginary dipole moments (Figure 6), showcasing the variation in the dipole strength (arrow length) and direction. Structural disorder also produces large variations in near-field intensities, with cold spots emerging where particles are further apart and intense hot spots in narrower gaps. As expected, dipole and NFE variations decrease as perfect ordering (Figure 6d) is approached. These observations agree with previous studies where structural defects in lattices led to an increased maximum near-field intensity. Although disorder increases the maximum enhancement at the most intense hot

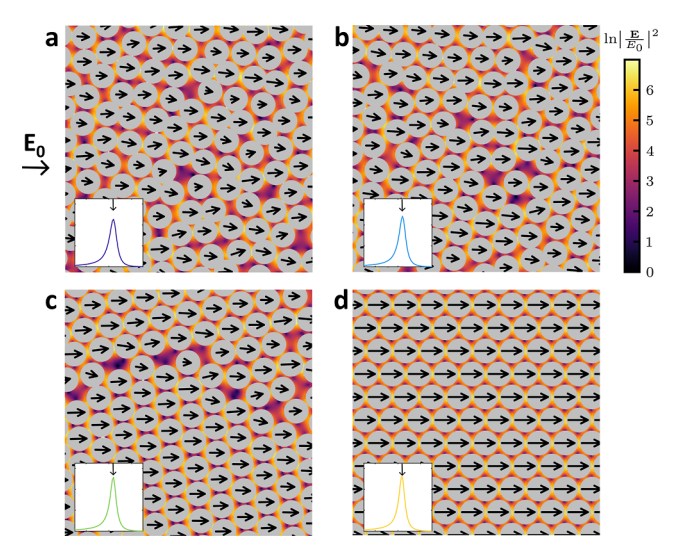


Figure 6. Near-field intensity maps of superlattice configurations, with arrows on particles indicating relative (within a configuration) strength of the imaginary dipole and its direction. Windows show only a small representative fraction of the 8100 nanoparticles. Field polarization  $E_0$  is in the direction indicated, parallel to the monolayer, and near-field properties are calculated at the ensemble extinction peak frequency for the respective configuration (indicated in insets). Maps correspond to configurations the following local bond-orientational order parameters ( $\Psi_{6,local}$ ): (a) 0.66, (b) 0.79, (c) 0.95, and (d) 1.

spots in the configurations, the spatially averaged near-field intensity decreases with decreasing order (Figure S9).

While spatially averaged near field enhancement provides one metric of how structural disorder impacts the near field, many applications such as SERS and SEIRA rely more specifically on hot spots at the surface of particles for detection of analytes in the gaps between particles. 1,59 We computed the distribution of hot spots within a given monolayer at its average resonance frequency (Figure 7a). Similar to the peak frequency distribution, the distribution of hot spots is broadest for the greatest disorder and narrows as order increases. Notably, the distributions for disordered monolayers have a substantial population of hot spots (10-50%) exceeding the magnitude of those in a perfectly ordered lattice. We find that an individual particle's hot spot intensity strongly correlates with its peak frequency. In fact, the approximately singlevalued function relating these two quantities (Figure 7b, inset) is universal in that it pertains to monolayers with different degrees of structural order. The direct effect of disorder is to broaden the distribution of individual nanoparticle resonant frequencies based on their heterogeneous local environments; the distribution of hot spot intensities directly reflects these variations in particle-level resonant frequencies.

Analysis of the optical response of individual particles established a correlation between each particle's peak frequency and the near-field enhancement in its adjacent hot spot. Each particle's frequency shift occurs due to its local structure, but now we seek to understand the specific attributes of the local structure near a hot spot and the hot spot's intensity. We evaluated the following features' roles in determining hot spot intensity: average distance from a particle to its neighbors  $(d_{avg})$ , angle between the vector pointing from the particle center to the hot spot and the direction of field polarization  $(\Theta_{hs})$ , the particle-level hexatic order  $(\Psi_6)$ , and

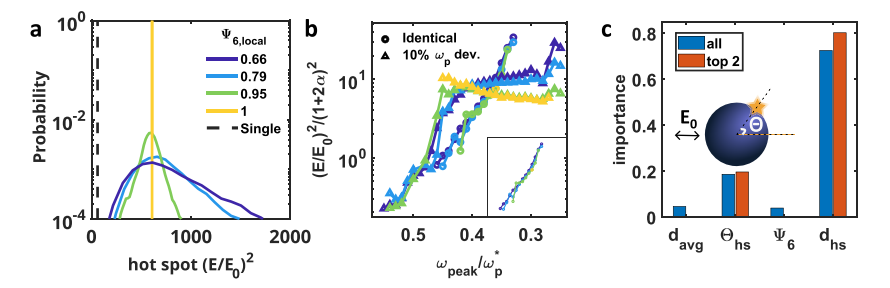
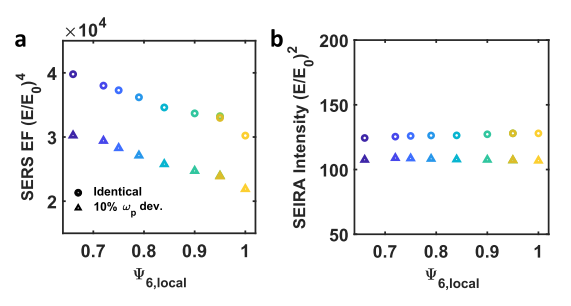


Figure 7. (a) Probability distribution of hot spots for the sequence of simulated superlattice monolayers with different average local bondorientation order  $\Psi_{6,local}$ . The hot spot of a single, isolated particle is included for reference. (b) Particle hot spot intensity, scaled by the maximum hot spot intensity for each isolated particle  $(1 + 2\alpha)^2$ , versus particle peak frequency, scaled by each particle's individual plasma frequency  $\omega_p^*$ , comparing (circles) identical particles and (triangles) particles with 10% plasma frequency deviation as in Figure 4b,c. Inset: identical particles alone. (c) Relative feature importance in a random forest regression for particle hot spots, ranked by mean decrease in impurity, using 4 descriptors (blue) or only the top 2 (orange). Features are as follows: average distance from neighbors  $(d_{avg})$ , angle of hot spot  $(\Theta_{hs})$  relative to field polarization, particle hexatic order  $(\Psi_6)$ , and distance to neighbor nearest to the hot spot  $(d_{hs})$ .

the distance to the neighbor closest to the hot spot  $(d_{\rm hs})$ . Using the mean decrease in impurity metric of a random forest regressor to predict hot spot intensity, we identified  $d_{\rm hs}$  and  $\Theta_{\rm hs}$  as the most significant features, with the hottest spots being correlated to a close neighbor aligned with the field polarization (Figure 7c). While distance is the most significant of the two factors, hot spot alignment with the polarization direction also plays a significant role.

We also considered particles with a realistic (i.e., 10%) distribution of particle plasma frequencies, as was done in Figure 4b,c to compare the influence of structural disorder and particle-level heterogeneity on near-field effects. The particle peak frequency and hot spot intensity are still correlated, but the slope of the line describing their correlation is lower, especially for the most ordered assemblies where local composition may be a stronger determinant of resonant frequency and hot spot intensity than local structure (Figure \$10). Indeed, we find an overall weakened correlation between local structure and particle resonant frequency based on the random forest analysis (Figure S11 and Table S5). We sought to analyze the distinct impacts of local composition and local structure by eliminating the direct effect that each particle's  $\omega_n$ has on its resonant frequency and the intensity of the adjacent hot spot. Specifically, each particle's hot spot intensity was normalized by the maximum hot spot intensity of an isolated particle with that dielectric function  $(1 + 2\alpha)^2 E_0$ , which occurs at its maximum dipole polarizability  $\alpha$ , and each individual resonant frequency in the assembly was normalized by the particle's plasma frequency  $\omega_p^*$  (Figure 7b). This scaling reveals how the NFE and resonant frequency are modified in the assembled structure from their values for the same particle in isolation. For a structurally perfect lattice with compositional disorder (yellow triangles), relative hot spot enhancement is weakly dependent on resonant frequencies, dropping slightly for more red-shifted resonances. With the introduction of structural disorder, the slopes of the correlations remain low but shift toward the relationship found for assemblies of identical particles. For the highest resonant frequencies, where the NFE is very weak, the trends collapse for both the identical particle and heterogeneous particle cases, suggesting that these particles are poorly coupled in the assemblies. The slope of the correlations in Figure 7b thus highlights the trade-off between the impacts of structural disorder and compositional disorder, which are both present in realistic assemblies, on local hot spot intensities.

Finally, we considered how the variations in monolayer structural disorder and NFE influence predicted properties relevant for detection in SERS and SEIRA applications. Specifically, we calculated the surface-averaged SERS enhancement at zero Raman shift  $(|E/E_0|^4)$  at the ensemble resonant peak frequency for each simulated monolayer configuration (Figure 8a). Instead of focusing on the most intense hot spot



**Figure 8.** Effects of local bond-orientational order in simulated monolayers for (a) surface-averaged SERS enhancement factor at zero Raman shift  $|E/E_0|^4$  and (b) surface-averaged SEIRA intensity enhancement  $|E/E_0|^2$ , comparing (circles) identical particles and (triangles) particles with 10% plasma frequency deviation.

on each particle, field intensities at evenly spaced points over each nanoparticle's spherical surface were probed. Each value was squared, and then all values within the configuration were averaged to approximate the monolayer's SERS enhancement under macroscopic detection conditions. While the field intensities provide an estimate of the enhancement, it is important to note that additional factors we do not account for, such as short-range charge transfer, can contribute to total SERS enhancement.<sup>60</sup> In general, as structural order decreased from the value for a perfect lattice ( $\Psi_6 = 1$ ), SERS enhancement increased. This predicted behavior remained unchanged when a 10% deviation in nanoparticle plasma frequencies was included (Figure 8a), although the magnitude of the enhancement factors decreased by ~25% as compared to a compositionally uniform monolayer with the same structure. Further, more disordered monolayers had larger magnitudes of maximum SERS hot spot enhancement by up to 2 orders of magnitude compared to the perfect lattice (Figure S12). These singular intensities could be advantageous for some applications, though there is also value in having a large number of uniform hot spots with a given intensity for

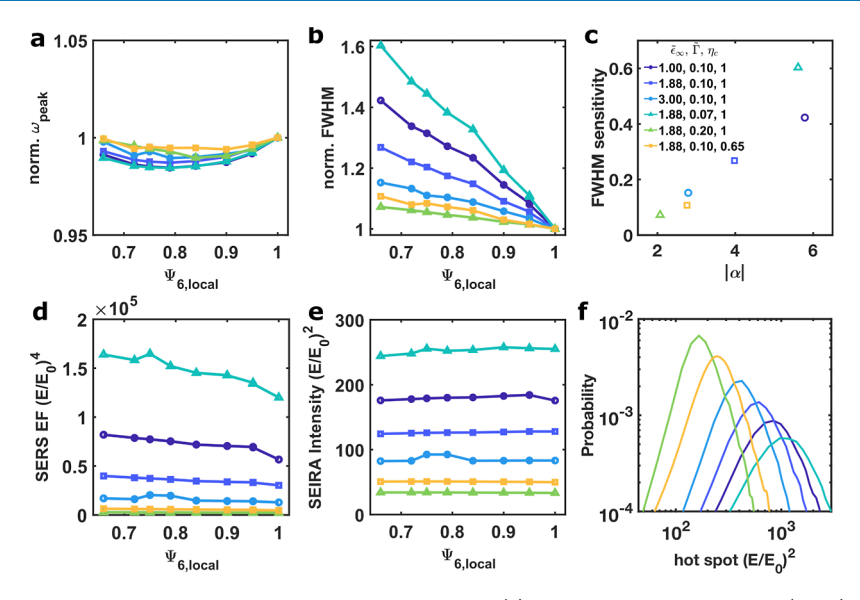


Figure 9. Normalized sensitivity to average local bond-orientational order for (a) extinction peak frequency ( $\omega_{\text{peak}}$ ), (b) extinction peak width (fwhm) for varying high-frequency dielectric constant ( $\tilde{\epsilon}_{\infty} = \epsilon_{\infty}/\epsilon_m$ ), damping ( $\tilde{\Gamma} = \gamma/\omega_p^*$ ), and electron accessible volume fraction ( $\eta_c$ ). Quantities normalized to ensure perfect lattice properties are unity. (c) Sensitivity of extinction peak fwhm to bond-orientational order for each material dielectric function, defined as the fraction change from a perfect lattice to the most disordered considered ( $\Psi_{6,\text{local}} = 0.66$ ), as a function of maximum dipole polarizability  $|\alpha|$ . (d) Surface-averaged SERS enhancement factor at zero Raman shift  $|E/E_0|^4$  for each material dielectric function as a function of local order. (e) Surface-averaged SEIRA intensity enhancement  $|E/E_0|^2$  for each material dielectric function as a function of local order. (f) Probability distribution of hot spot intensities for each material for the configuration with  $\Psi_{6,\text{local}} = 0.66$ .

ensemble sensing, which has motivated using plasmonic arrays or superlattices as SERS platforms.  $^{61}$ 

SEIRA enhancement increases with near-field intensity (I instead of  $I^2$ ) and relies on structures with dense packing to generate small gaps and a high density of hot spots. 62,63 In our simulated monolayers, we observe a robust tolerance to disorder with enhancement remaining approximately unchanged across the full range of disorder, with only a slight reduction when a 10% variation in nanoparticle plasma frequency was included (Figure 8b). In addition, the introduction of particle diameter polydispersity does not significantly impact enhancement factors for either SERS or SEIRA when comparing configurations with similar average bond-orientational order (Figure S13). Overall, these calculations indicate that a wide range of dense monolayer structures would produce similar spectroscopic enhancement, with significantly disordered monolayers exhibiting comparable behavior for SEIRA and some potential benefits for the detection limits in SERS applications.

Influence of Material Dielectric Parameters. How structural disorder influences the optical response of our model monolayers is qualitatively similar for nanoparticles modeled with a Drude dielectric function regardless of the electron accessible volume fraction, damping, or highfrequency dielectric constant. The ensemble peak frequency for the plasmon resonance of the monolayer is insensitive to the extent of structural disorder present, and peak broadening increases for more disordered superlattices (Figure 9a,b). The sensitivity of a superlattice's optical response to disorder depends on nanoparticle composition. Materials with stronger LSPR coupling interactions, such as those with low damping, display higher sensitivity. These materials are distinguished by their high quality or Q-factor, defined as the ratio of the LSPR peak frequency to the fwhm. All other factors equal, nanoparticles with an electron depletion layer at their surface

(common for nanocrystals composed of doped metal oxides such as tin-doped indium oxide, aluminum-doped zinc oxide, and indium-doped cadmium oxide), 54,64 leading to electron accessible volume fractions ( $\eta_c$ ) less than one, have weaker LSPR coupling because their free electrons are effectively further apart. As a result, superlattices of such nanoparticles have properties that are less sensitive to changes in the structural order.

The sensitivity of peak broadening to structural disorder is most significantly affected by the nanoparticle polarizability (Figure 9c). We observe that sensitivity, as measured by, e.g., the percentage change in fwhm from perfect to most disordered structures, grows with increasing maximum dipole polarizability  $|\alpha|$ . This makes intuitive sense as particles with the greatest polarizability are the most sensitive to environmental changes and, consequently, superlattice imperfections or defects. We calculated the maximum dipole polarizability for common metal nanoparticles to rank their defect sensitivity (Table 1). For high-Q-factor (low damping in Figure 9) building blocks, e.g., silver nanoparticles, the degree of structural disorder in the monolayer will more strongly affect the trade-off between narrow extinction peaks (favored by

Table 1. Maximum Dipole Polarizability ( $|\alpha|$ ) for Common Nanoparticle Compositions, in Vacuum ( $\varepsilon_{\rm m}=1$ ) and in Organic Ligand ( $\varepsilon_{\rm m}=2.1$ ) as Used Throughout This Study<sup>a</sup>

material	$ \alpha (\varepsilon_m=1)$	$ \alpha (\varepsilon_m = 2.1)$
aluminum	13.6	14.1
ITO	2.2	4.0
silver	8.2	263.4
titanium nitride	1.4	1.9
gold	1.8	3.4

<sup>&</sup>lt;sup>a</sup>Dielectric functions from literature for silver, gold, aluminum,  $^{70}$  and titanium nitride.  $^{71}$ 

ordering) and higher near-field enhancement required for applications like SERS (enhanced by disorder). Similarly, particles with lower high-frequency dielectric constants (Figure 9), e.g., aluminum nanoparticles, are also expected to exhibit defect sensitivity, though to a lesser extent.

For a given amount of structural order, differences in material dielectric function parameters change the shape and magnitude of the hot spot distribution (Figure 9d-f). While higher Q-factor particles have distributions shifted toward more intense hot spots and higher SERS enhancement factors (Figure 9d), they also have the broadest hot spot distribution due to their sensitivity to disorder. Broad distributions of hot spots can hinder reproducibility in SERS experiments, which argues for regular structures with uniform spacing, but detection of analytes at low concentrations requires sufficient SERS enhancement. This motivates the choice of a material with more structural uniformity, provided it has hot spot intensities that are sufficiently high for a given molecular detection application.

Finally, though superlattices have somewhat limited structural tunability, e.g., compared to nanoparticle gel networks, which can support a continuous range of average coordination number and accommodate building blocks with different shapes and sizes, <sup>28,66,67</sup> these assemblies still have considerable customizability through the choice of building block composition. For example, doped metal oxide nanocrystals of the same shape and size, but different dopant concentrations, can be synthesized with LSPR across the near-and mid-IR, <sup>68</sup> so compositionally distinct nanocrystals can be randomly mixed together in different ratios to assemble superlattice metamaterials for a variety of targeted photonic applications. <sup>36,69</sup>

#### CONCLUSIONS

The modeling presented here predicts that the primary effect of structural disorder in 2D superlattices of metal nanoparticles is to broaden the distribution of local particle environments and, consequently, particle-level resonant frequencies. Wide distributions of hot spot intensities can emerge, correlating with the individual particles' plasmon frequencies. While it is appreciated that hot spot intensity is strongly influenced by the proximity of a hot spot's nearest neighbors, we demonstrate that the angle of a particle's hot spot with respect to the field polarization is also important. In monolayers with intermediate levels of structural order present, intense hot spots form in the gaps between particle pairs or in multiparticle chains aligned parallel to the field polarization, with resonant frequencies redshifted relative to the ensemble peak position. In more ordered films, structural and hence local resonant frequency deviations concentrate at grain boundaries or other defects to produce intense hot (and cold) spots.

Extinction fwhm and SERS enhancement factors monotonically increase with the extent of structural disorder present, though the latter does not strongly affect the monolayer extinction peak frequency or field intensity for SEIRA. Dipole polarizability of the nanoparticles primarily sets the spectroscopic enhancement and defect sensitivity of the resulting assemblies. Due to the tolerance of extinction peak frequency to defects, for applications where a targeted peak resonance is desired (e.g., radiative cooling/thermal management, electrochromics, etc.), <sup>69,72,73</sup> disordered or partially ordered films could be a viable and more time and cost-effective alternative to highly ordered superlattices, provided that disorder-induced

broadening does not diminish peak heights below what is required for performance in an integrated photonic device. For applications where success is measured by near-field enhancement (e.g., molecular sensing and detection), 59,74 the presence of some defects in an ordered lattice may even be desirable to generate high enhancement factors and increase sensitivity to the presence of analytes. However, there may be an optimal amount of disorder to target high near fields with a modest spread to maintain reproducibility.

While it is challenging to assemble a superlattice with targeted defectivity in the lab, experimental assembly protocol optimization could be guided by postassembly structural characterization, e.g., via electron microscopy image analysis using deep learning algorithms. However, because the concentration of structural defects is difficult to control experimentally and defects are nearly impossible to eliminate, material composition provides the primary design parameter for tuning superlattice properties for many applications. The sensitivity of extinction peak width and SERS enhancement to particle-level heterogeneity highlights the importance of developing scalable synthetic strategies for preparing uniform, high-quality nanoparticles with targeted characteristics for integration into superstructures for photonic applications. <sup>14,15,55,56</sup>

The trends presented here should generally hold for plasmonic nanoparticles, although our experimental comparisons with ITO nanocrystal monolayers highlight the importance of accounting for electron depletion layers and variation in nanoparticle plasma frequency. These characteristics weaken the linkage between the local structure and particle-level resonant frequency in the resulting assemblies, but they do not qualitatively change the optical properties of the resulting 2D superlattices.

While the optical response of experimental monolayers maps onto the simulation trends presented here, more comprehensive comparisons are needed. There are also limitations to our modeling. The MPM simulations do not account for higher order moments (i.e., quadrupoles, octupoles, etc.), which we expect to be present but may have minor contributions in disordered monolayers as these systems are dipole-dominated due to their symmetry.<sup>20</sup> Further work would be required to extend MPM to treat monolayers of faceted particles and explore the impact of shape on defect tolerance. S Rich phase behavior has been observed for monolayers of mixed squares and disks, exhibiting both hexatic and tetratic order,<sup>75</sup> and materials like these may lead to distinctive optical properties. Mixed monolayers of identically shaped (spherical) particles with different dielectric parameters have already been shown to exhibit tunable optical behavior and are worthy of further investigation. 35,36,76 While this study closely examined monolayers and the bright collective plasmon mode, extending the simulations beyond the quasistatic approximation and conducting similar analyses for bilayers and multilayer films could help clarify the mechanisms by which different types of disorder impact plasmon-polariton modes observed in 3D superlattice studies. 14,16

# METHODS

**Brownian Dynamics Simulation Methods.** We performed 2D Brownian dynamics simulations using HOOMD-Blue v2.9.7.<sup>77</sup> Particles interacted with hard sphere repulsion

$$U_{\rm hs} = \frac{\gamma_{\rm h}}{4\Delta t} (r - 2a)^2, \qquad r < 2a \tag{1}$$

where  $\gamma_h$  is the Stokes–Einstein hydrodynamic drag coefficient, a is the particle radius,  $\Delta t$  is the time step of  $10^{-4}\tau_{\rm D}$ , and  $\tau_{\rm D}$  is the diffusion time of a particle  $(\tau_D = \gamma_h a^2/k_B T)$ . When two particles overlap, this potential resets them to contact at the next time step, which is an implementation of the Heyes-Melrose hard-sphere algorithm.<sup>78</sup> The simulations were performed with 8100 particles in a periodically replicated 2D cell. The particles were compressed from an area fraction of 0.2 to  $\approx 0.9$  with varying compression times (Table S1), where particle ordering increases with a longer compression time (slower compression rate). We used freud for structural analysis including computing bond orientational order parameters  $\Psi_{6,m} = \frac{1}{N_b} \sum_{n=1}^{N_b} e^{6i\Theta_{mn}}$ , where  $N_b$  is a particle's number of neighbors, defined here as Voronoi neighbors, and  $\Theta_{mn}$  is the angle between a pair of particles and an arbitrary axis. From the bond orientational order parameter, the local order parameter is defined as  $\Psi_{6,local} = \langle |\Psi_{6m}| \rangle$ , averaging over central particles and configurations.

**Optical Simulations: MPM.** We performed optical simulations using MPM, enabling efficient calculations for complex assemblies with large numbers of particles in periodic boundary conditions. MPM code is available at github.com/zeesherman/mutual-polarization. Briefly, MPM uses a matrix-free, spectrally accurate Ewald summation to solve a linear system of equations for a system of coupled dipoles  $(\mathbf{p}_i)$  for i particles

$$\mathbf{E}_{0} = \sum_{j} \mathbf{M}_{ij} \cdot \mathbf{p}_{j} \qquad \mathbf{M}_{ij} = \begin{cases} \frac{\mathbf{I}}{4\pi a^{3} \varepsilon_{m} \alpha}, & i = j \\ \frac{\mathbf{I} - 3\hat{\mathbf{r}}\hat{\mathbf{r}}}{4\pi \varepsilon_{m} r^{3}}, & i \neq j \end{cases}$$
(2)

where a is the radius of the optical core,  $\mathbf{E}_0$  is the electric field polarization,  $\alpha=(\varepsilon_{\rm p}-\varepsilon_{\rm m})/(\varepsilon_{\rm p}+2\varepsilon_{\rm m})$  is the dipole polarizability,  $\varepsilon_{\rm p}$  is a particle's permittivity,  $\varepsilon_{\rm m}$  is the medium's permittivity (here, a constant ligand permittivity),  $\mathbf{r}=\mathbf{x}_i-\mathbf{x}_j$ ,  $\mathbf{x}_i$  is position of particle  $i, r=|\mathbf{r}|$ , and  $\hat{\mathbf{r}}=r/r$ . From the solution of coupled dipoles, we then calculated quantities, including extinction, reflection, and near-field intensity.

Particle permittivity was modeled using a Drude dielectric function (Table 2)

$$\varepsilon_{\rm p} = \varepsilon_{\infty} - \frac{\varepsilon_0 \omega_{\rm p}^2}{\omega^2 + i\gamma\omega} \tag{3}$$

except for one case in Figure 9 where, to describe an electron depletion layer, a core-shell Drude dielectric function was used

Table 2. Parameters Used in MPM Simulations Throughout the Main Text, Except Where Noted in Figure 9

Quantity	
drude $\omega_{\mathrm{p}}~(\mathrm{cm}^{-1})$	15,000
drude $\gamma/\omega_{ m p}^*$	0.10
drude $\epsilon_{\infty}/\epsilon_0$	4.00
background $arepsilon_{ m m}/arepsilon_0$	2.13
core fraction $\eta_c$	1.00

$$\varepsilon_{p} = \varepsilon_{s} \frac{\varepsilon_{c} + \varepsilon_{s} + 2\eta_{c}(\varepsilon_{c} - \varepsilon_{s})}{\varepsilon_{c} + 2\varepsilon_{s} - \eta_{c}(\varepsilon_{c} - \varepsilon_{s})},$$

$$\varepsilon_{c} = \varepsilon_{\infty} - \frac{\varepsilon_{0}\omega_{p}}{\omega^{2} + i\gamma\omega}, \qquad \varepsilon_{s} = \varepsilon_{\infty}$$
(4)

here,  $\varepsilon_{\infty}$  is the high frequency dielectric constant,  $\omega_{\rm p}$  is the plasma frequency,  $\omega$  is the frequency,  $\gamma$  is the damping,  $\varepsilon_{\rm c}$  is the core permittivity,  $\varepsilon_{\rm s}$  is the shell permittivity, and  $\eta_{\rm c}$  is the electron accessible volume fraction.

Implementation of Neural Networks. *Cellpose*. We analyzed SEM images of nanocrystal monolayers using Cellpose, a neural network designed for cellular segmentation. This algorithm works by analyzing spatial gradients in images to create masks and subsequently outlines the separation of objects in the image. It combines a U-Net, with convolutional maps, and has been trained on large and highly varied data sets. The cytoplasm model was used, and no additional training was required. We extracted the centroids of each particle and then analyzed their structural order, applying the same analysis methods used to structurally evaluate our molecular dynamics simulations.

Random Forest Regression. We implemented the random forest regressor from scikit-learn <sup>81</sup> (version 1.3.0) to determine the importance of physical descriptors on a particle's maximum hot spot intensity. To fit the model, 100 estimators were used and we used the default for the remaining parameters. The mean decrease in impurity metric was used to estimate each feature's importance within the model, where importance values are normalized so they sum to one.

**Experimental Methods.** We did not take any extra purification steps for any of the chemicals. Indium(III) acetate (99.99%, STREM), tin(IV) acetate (Sigma-Aldrich), oleic acid (OA, 90%, technical grade, Sigma-Aldrich), oleyl alcohol (OLA, 90%, technical grade, Sigma-Aldrich), and octadecene (ODE, 85%, technical grade) were used to synthesize the NCs. We used hexane (98%, Sigma-Aldrich) and toluene (99.8%, Sigma-Aldrich) to disperse the nanocrystals for forming nanocrystal monolayers.

Nanocrystals were synthesized using the slow injection method. We first dissolved  $8 \times (1 - x)$  mmol of indium acetate and x mmol of tin acetate in 16 mL of OA and 8 mL of ODE. Here, x is equivalent to 0.01, 0.03, and 0.06 for 1, 3, and 6% Sn-doped ITO nanocrystals, respectively. We then heated this metal precursor solution to 160 °C for 2 h under a nitrogen environment. In a separate flask, 13 mL of the OLA was degassed under vacuum for 1 h at 130 °C. Then, the OLA flask was heated up to 290 °C under a nitrogen environment. Once the set point temperature of the OLA flask was reached, using a 50 mL glass syringe, we injected 21 mL of the metal precursor with an injection rate of 0.3 mL min<sup>-1</sup> into the OLA solution using a syringe pump. Once the injection was complete, we waited for 20 min at 290 °C and then started cooling down until it reached room temperature by removing the heating mantle. We then washed the product with hexane (for dispersing nanocrystals) and ethanol (for precipitation) three times by centrifugation and redispersed it in 20 mL of

The ITO nanocrystal monolayer preparation method was fully described in our previous work. We sonicated a  $2 \times 2$  cm<sup>2</sup> double-side polished undoped silicon wafer for one h in a 1% Hellmanex III aqueous solution and acetone. Then, we dropped 200  $\mu$ L of deionized water onto the substrate and

sequentially added 100  $\mu$  L of a 1 mg mL<sup>-1</sup> ITO nanocrystal dispersion (in hexane/toluene = 2:1 by volume) on top of the water droplet. A glass slide was used to control the evaporation rate of the organic solvent. After evaporation of the organic solvent layer, we uncovered the sample to allow the water to evaporate, leaving the nanocrystal monolayer resting on the silicon wafer.

The local area transmission measurements of the ITO nanocrystal monolayers were conducted by using a Hyperion 2000 IR microscope (Bruker) attached to the V70 FT-IR spectrometer (Bruker) with a liquid nitrogen-cooled LN MCT detector. All measurements were performed using a Cassegrain objective with 36× magnification. For the transmission measurement, we used a bare silicon wafer as a reference. For larger area FT-IR measurement and solution phase measurement (NC dispersed in hexane with 0.5 mm thick spacer), we used a Bruker Vertex 70 Fourier transform IR spectrometer and Agilent Cary 5000 UV—vis—NIR spectrometer with transmission geometry. Microscopic NC monolayer images were measured using a Hitachi S5500 scanning transmission electron microscope under secondary electron modes.

#### ASSOCIATED CONTENT

# Supporting Information

The Supporting Information is available free of charge at https://pubs.acs.org/doi/10.1021/acsphotonics.3c01813.

Additional description of computational methods, characterization of simulation configurations and experimental images, and analysis details (PDF)

## AUTHOR INFORMATION

#### **Corresponding Authors**

Delia J. Milliron — McKetta Department of Chemical Engineering, University of Texas at Austin, Austin, Texas 78712, United States; ○ orcid.org/0000-0002-8737-451X; Email: milliron@che.utexas.edu

Thomas M. Truskett — McKetta Department of Chemical Engineering, University of Texas at Austin, Austin, Texas 78712, United States; Department of Physics, University of Texas at Austin, Austin, Texas 78712, United States; orcid.org/0000-0002-6607-6468; Email: truskett@che.utexas.edu

#### **Authors**

Allison M. Green — McKetta Department of Chemical Engineering, University of Texas at Austin, Austin, Texas 78712, United States; orcid.org/0000-0002-7734-4202

Woo Je Chang — McKetta Department of Chemical Engineering, University of Texas at Austin, Austin, Texas 78712, United States

Zachary M. Sherman – McKetta Department of Chemical Engineering, University of Texas at Austin, Austin, Texas 78712, United States; orcid.org/0000-0001-9798-287X

Zarko Sakotic — Department of Electrical and Computer Engineering, University of Texas at Austin, Austin, Texas 78712, United States; Oorcid.org/0000-0003-3886-1378

Kihoon Kim — McKetta Department of Chemical Engineering, University of Texas at Austin, Austin, Texas 78712, United States; ◎ orcid.org/0000-0003-1034-9233 Daniel Wasserman — Department of Electrical and Computer Engineering, University of Texas at Austin, Austin, Texas 78712, United States; orcid.org/0000-0003-3234-0803

Complete contact information is available at: https://pubs.acs.org/10.1021/acsphotonics.3c01813

#### Notes

The authors declare no competing financial interest.

#### ACKNOWLEDGMENTS

This work was primarily supported by the National Science Foundation through the Center for Dynamics and Control of Materials: an NSF Materials Research Science and Engineering Center (NSF MRSEC) under Cooperative Agreements DMR-1720595 and DMR-2308817. Research was also sponsored by the Army Research Office and was accomplished under Grant Number W911NF-23-1-0387. D.J.M. and T.M.T. acknowledge support from the Welch Foundation (F-1848 and F-1696). Z.S. and D.W. acknowledge support from the Defense Advanced Research Projects Agency (DARPA) under the Optomechanical Thermal Imaging (OpTIm) program (HR00112320022). The authors acknowledge the Texas Advanced Computing Center (TACC) for providing computing resources that contributed to the research results reported in this paper.

# REFERENCES

- (1) Solís, D. M.; Taboada, J. M.; Obelleiro, F.; Liz-Marzán, L. M.; García de Abajo, F. J. Optimization of Nanoparticle-Based SERS Substrates through Large-Scale Realistic Simulations. *ACS Photonics* **2017**, *4*, 329–337.
- (2) Mueller, N. S.; Pfitzner, E.; Okamura, Y.; Gordeev, G.; Kusch, P.; Lange, H.; Heberle, J.; Schulz, F.; Reich, S. Surface-Enhanced Raman Scattering and Surface-Enhanced Infrared Absorption by Plasmon Polaritons in Three-Dimensional Nanoparticle Supercrystals. *ACS Nano* **2021**, *15*, 5523–5533.
- (3) Murray, C. B.; Kagan, C. R.; Bawendi, M. G. Synthesis and Characterization of Monodisperse Nanocrystals and Close-packed Nanocrystal Assemblies. *Annu. Rev. Mater. Sci.* **2000**, *30*, 545–610.
- (4) Klinkova, A.; Choueiri, R. M.; Kumacheva, E. Self-assembled Plasmonic Nanostructures. *Chem. Soc. Rev.* **2014**, *43*, 3976–3991.
- (5) Korgel, B. A.; Fitzmaurice, D. Condensation of Ordered Nanocrystal Thin Films. *Phys. Rev. Lett.* **1998**, *80*, 3531–3534.
- (6) Tao, A.; Sinsermsuksakul, P.; Yang, P. Tunable Plasmonic Lattices of Silver Nanocrystals. *Nat. Nanotechnol.* **2007**, *2*, 435–440.
- (7) Dong, A.; Ye, X.; Chen, J.; Murray, C. B. Two-dimensional Binary and Ternary Nanocrystal Superlattices: The Case of Monolayers and Bilayers. *Nano Lett.* **2011**, *11*, 1804–1809.
- (8) Bigioni, T. P.; Lin, X.-M.; Nguyen, T. T.; Corwin, E. I.; Witten, T. A.; Jaeger, H. M. Kinetically Driven Self Assembly of Highly Ordered Nanoparticle Monolayers. *Nat. Mater.* **2006**, *5*, 265–270.
- (9) Wen, T.; Majetich, S. A. Ultra-large-area Self-assembled Monolayers of Nanoparticles. ACS Nano 2011, 5, 8868–8876.
- (10) Weidman, M. C.; Nguyen, Q.; Smilgies, D.-M.; Tisdale, W. A. Impact of Size Dispersity, Ligand Coverage, and Ligand Length on the Structure of PbS Nanocrystal Superlattices. *Chem. Mater.* **2018**, 30, 807–816.
- (11) Shevchenko, E. V.; Talapin, D. V.; Kotov, N. A.; O'Brien, S.; Murray, C. B. Structural Diversity in Binary Nanoparticle Superlattices. *Nature* **2006**, 439, 55–59.
- (12) Whitham, K.; Smilgies, D.-M.; Hanrath, T. Entropic, Enthalpic, and Kinetic Aspects of Interfacial Nanocrystal Superlattice Assembly and Attachment. *Chem. Mater.* **2018**, *30*, 54–63.
- (13) Zhou, Y.; Arya, G. Discovery of Two-dimensional Binary Nanoparticle Superlattices Using Global Monte Carlo Optimization. *Nat. Commun.* **2022**, *13*, 7976.

- (14) Schulz, F.; Pavelka, O.; Lehmkühler, F.; Westermeier, F.; Okamura, Y.; Mueller, N. S.; Reich, S.; Lange, H. Structural Order in Plasmonic Superlattices. *Nat. Commun.* **2020**, *11*, 3821.
- (15) Schulz, F.; Lokteva, I.; Parak, W. J.; Lehmkühler, F. Recent Notable Approaches to Study Self-Assembly of Nanoparticles with X-Ray Scattering and Electron Microscopy. *Part. Part. Syst. Char.* **2021**, 38, 2100087.
- (16) Mueller, N. S.; Vieira, B. G. M.; Schulz, F.; Kusch, P.; Oddone, V.; Barros, E. B.; Lange, H.; Reich, S. Dark Interlayer Plasmons in Colloidal Gold Nanoparticle Bi- and Few-Layers. *ACS Photonics* **2018**, *5*, 3962–3969.
- (17) Mueller, N. S.; Vieira, B. G.; Höing, D.; Schulz, F.; Barros, E. B.; Lange, H.; Reich, S. Direct Optical Excitation of Dark Plasmons for Hot Electron Generation. *Faraday Discuss.* **2019**, *214*, 159–173.
- (18) Mueller, N. S.; Okamura, Y.; Vieira, B. G. M.; Juergensen, S.; Lange, H.; Barros, E. B.; Schulz, F.; Reich, S. Deep Strong Light—matter Coupling in Plasmonic Nanoparticle Crystals. *Nature* **2020**, 583, 780–784.
- (19) Arul, R.; Grys, D.-B.; Chikkaraddy, R.; Mueller, N. S.; Xomalis, A.; Miele, E.; Euser, T. G.; Baumberg, J. J. Giant Mid-IR Resonant Coupling to Molecular Vibrations in Sub-nm Gaps of Plasmonic Multilayer Metafilms. *Light Sci. Appl.* **2022**, *11*, 281.
- (20) Ross, M. B.; Ku, J. C.; Blaber, M. G.; Mirkin, C. A.; Schatz, G. C. Defect Tolerance and the Effect of Structural Inhomogeneity in Plasmonic DNA-nanoparticle Superlattices. *Proc. Natl. Acad. Sci. U.S.A.* 2015, 112, 10292–10297.
- (21) Bagiński, M.; Pedrazo-Tardajos, A.; Altantzis, T.; Tupikowska, M.; Vetter, A.; Tomczyk, E.; Suryadharma, R. N.; Pawlak, M.; Andruszkiewicz, A.; Górecka, E.; et al. Understanding and Controlling the Crystallization Process in Reconfigurable Plasmonic Superlattices. *ACS Nano* **2021**, *15*, 4916–4926.
- (22) Auguié, B.; Barnes, W. L. Diffractive Coupling in Gold Nanoparticle Arrays and the Effect of Disorder. *Opt. Lett.* **2009**, *34*, 401–403.
- (23) Ponomareva, E.; Volk, K.; Mulvaney, P.; Karg, M. Surface Lattice Resonances in Self-Assembled Gold Nanoparticle Arrays: Impact of Lattice Period, Structural Disorder, and Refractive Index on Resonance Quality. *Langmuir* **2020**, *36*, 13601–13612.
- (24) Zhang, F.; Tang, F.; Xu, X.; Adam, P.-M.; Martin, J.; Plain, J. Influence of Order-to-disorder Transitions on the Optical Properties of the Aluminum Plasmonic Metasurface. *Nanoscale* **2020**, *12*, 23173–23182.
- (25) Bohren, C. F.; Huffman, D. R. Absorption and Scattering of Light by Small Particles; John Wiley & Sons, 2008.
- (26) Jain, P. K.; Huang, W.; El-Sayed, M. A. On the Universal Scaling Behavior of the Distance Decay of Plasmon Coupling in Metal Nanoparticle Pairs: A Plasmon Ruler Equation. *Nano Lett.* **2007**, *7*, 2080–2088.
- (27) Liu, N.; Hentschel, M.; Weiss, T.; Alivisatos, A. P.; Giessen, H. Three-dimensional Plasmon Rulers. *Science* **2011**, 332, 1407–1410.
- (28) Kang, J.; Sherman, Z. M.; Conrad, D. L.; Crory, H. S. N.; Dominguez, M. N.; Valenzuela, S. A.; Anslyn, E. V.; Truskett, T. M.; Milliron, D. J. Structural Control of Plasmon Resonance in Molecularly Linked Metal Oxide Nanocrystal Gel Assemblies. ACS Nano 2023, 17, 24218–24226.
- (29) Zou, S.; Schatz, G. C. Narrow Plasmonic/Photonic Extinction and Scattering Line Shapes for One and Two Dimensional Silver Nanoparticle Arrays. *J. Chem. Phys.* **2004**, *121*, 12606–12612.
- (30) Lazarides, A. A.; Schatz, G. C. DNA-linked Metal Nanosphere Materials: Structural Basis for the Optical Properties. *J. Phys. Chem. B* **2000**, *104*, 460–467.
- (31) Mackowski, D. W.; Mishchenko, M. I. Calculation of the T Matrix and the Scattering Matrix for Ensembles of Spheres. *J. Opt. Soc. Am. A* **1996**, *13*, 2266–2278.
- (32) Antosiewicz, T. J.; Apell, S. P. Plasmonic Glasses: Optical Properties of Amorphous Metal-dielectric Composites. *Opt. Express* **2014**, *22*, 2031–2042.
- (33) Egel, A.; Czajkowski, K. M.; Theobald, D.; Ladutenko, K.; Kuznetsov, A. S.; Pattelli, L. SMUTHI: A Python Package for the

- Simulation of Light Scattering by Multiple Particles Near or Between Planar Interfaces. *J. Quant. Spectrosc. Radiat. Transfer* **2021**, 273, 107846
- (34) Theobald, D.; Beutel, D.; Borgmann, L.; Mescher, H.; Gomard, G.; Rockstuhl, C.; Lemmer, U. Simulation of Light Scattering in Large, Disordered Nanostructures Using a Periodic T-matrix Method. *J. Quant. Spectrosc. Radiat. Transfer* **2021**, 272, 107802.
- (35) Sherman, Z. M.; Kim, K.; Kang, J.; Roman, B. J.; Crory, H. S. N.; Conrad, D. L.; Valenzuela, S. A.; Lin, E. Y.; Dominguez, M. N.; Gibbs, S. L.; Anslyn, E. V.; Milliron, D. J.; Truskett, T. M. Plasmonic Response of Complex Nanoparticle Assemblies. *Nano Lett.* **2023**, 23, 3030–3037.
- (36) Kim, K.; Sherman, Z. M.; Cleri, A.; Chang, W. J.; Maria, J.-P.; Truskett, T. M.; Milliron, D. J. Hierarchically Doped Plasmonic Nanocrystal Metamaterials. *Nano Lett.* **2023**, 23, 7633–7641.
- (37) Singh, M.; Sherman, Z. M.; Milliron, D. J.; Truskett, T. M. Linker-Templated Structure Tuning of Optical Response in Plasmonic Nanoparticle Gels. *J. Phys. Chem. C* **2022**, *126*, 16885–16893
- (38) Kang, J.; Sherman, Z. M.; Crory, H. S. N.; Conrad, D. L.; Berry, M. W.; Roman, B. J.; Anslyn, E. V.; Truskett, T. M.; Milliron, D. J. Modular Mixing in Plasmonic Metal Oxide Nanocrystal Gels with Thermoreversible Links. *J. Chem. Phys.* **2023**, *158*, 024903.
- (39) Schreck, C. F.; O'Hern, C. S.; Silbert, L. E. Tuning Jammed Frictionless Disk Packings from Isostatic to Hyperstatic. *Phys. Rev. E* **2011**, *84*, 011305.
- (40) Zhong, Y.; Allen, V. R.; Chen, J.; Wang, Y.; Ye, X. Multistep Crystallization of Dynamic Nanoparticle Superlattices in Nonaqueous Solutions. *J. Am. Chem. Soc.* **2022**, *144*, 14915–14922.
- (41) Lehmkühler, F.; Schulz, F.; Schroer, M. A.; Frenzel, L.; Lange, H.; Grübel, G. Local Orientational Order in Self-assembled Nanoparticle Films: The Role of Ligand Composition and Salt. *J. Appl. Crystallogr.* **2019**, *52*, 777–782.
- (42) Lotito, V.; Zambelli, T. Pattern Detection in Colloidal Assembly: A Mosaic of Analysis Techniques. *Adv. Colloid Interface Sci.* **2020**, 284, 102252.
- (43) Kansal, A. R.; Truskett, T. M.; Torquato, S. Nonequilibrium Hard-disk Packings with Controlled Orientational Order. *J. Chem. Phys.* **2000**, *113*, 4844–4851.
- (44) Truskett, T. M.; Torquato, S.; Debenedetti, P. G. Towards a Quantification of Disorder in Materials: Distinguishing Equilibrium and Glassy Sphere Packings. *Phys. Rev. E* **2000**, *62*, 993–1001.
- (45) Stringer, C.; Wang, T.; Michaelos, M.; Pachitariu, M. Cellpose: A Generalist Algorithm for Cellular Segmentation. *Nat. Methods* **2021**, *18*, 100–106.
- (46) Gibbs, S. L.; Staller, C. M.; Agrawal, A.; Johns, R. W.; Saez Cabezas, C. A.; Milliron, D. J. Intrinsic Optical and Electronic Properties from Quantitative Analysis of Plasmonic Semiconductor Nanocrystal Ensemble Optical Extinction. *J. Phys. Chem. C* **2020**, *124*, 24351–24360.
- (47) Johns, R. W.; Bechtel, H. A.; Runnerstrom, E. L.; Agrawal, A.; Lounis, S. D.; Milliron, D. J. Direct Observation of Narrow Midinfrared Plasmon Linewidths of Single Metal Oxide Nanocrystals. *Nat. Commun.* **2016**, *7*, 11583.
- (48) Stietz, F.; Bosbach, J.; Wenzel, T.; Vartanyan, T.; Goldmann, A.; Träger, F. Decay Times of Surface Plasmon Excitation in Metal Nanoparticles by Persistent Spectral Hole Burning. *Phys. Rev. Lett.* **2000**, *84*, 5644–5647.
- (49) Machida, K.; Adachi, K. Particle Shape Inhomogeneity and Plasmon-band Broadening of Solar-control LaB<sub>6</sub> Nanoparticles. *J. Appl. Phys.* **2015**, *118*, 013103.
- (50) Noguez, C. Surface Plasmons on Metal Nanoparticles: The Influence of Shape and Physical Environment. *J. Phys. Chem. C* **2007**, *111*, 3806–3819.
- (51) Agrawal, A.; Kriegel, I.; Milliron, D. J. Shape-Dependent Field Enhancement and Plasmon Resonance of Oxide Nanocrystals. *J. Phys. Chem. C* 2015, 119, 6227–6238.

- (52) Kawasaki, T.; Tanaka, H. Structural origin of dynamic heterogeneity in three-dimensional colloidal glass formers and its link to crystal nucleation. *J. Phys.: Condens. Matter* **2010**, 22, 232102.
- (53) Cho, S. H.; Roccapriore, K. M.; Dass, C. K.; Ghosh, S.; Choi, J.; Noh, J.; Reimnitz, L. C.; Heo, S.; Kim, K.; Xie, K.; Korgel, B. A.; Li, X.; Hendrickson, J. R.; Hachtel, J. A.; Milliron, D. J. Spectrally Tunable Infrared Plasmonic F,Sn:In<sub>2</sub>O<sub>3</sub> Nanocrystal Cubes. *J. Chem. Phys.* **2020**, *152*, 014709.
- (54) Gibbs, S. L.; Staller, C. M.; Milliron, D. J. Surface Depletion Layers in Plasmonic Metal Oxide Nanocrystals. *Acc. Chem. Res.* **2019**, 52, 2516–2524.
- (55) Jansons, A. W.; Hutchison, J. E. Continuous Growth of Metal Oxide Nanocrystals: Enhanced Control of Nanocrystal Size and Radial Dopant Distribution. *ACS Nano* **2016**, *10*, 6942–6951.
- (56) Staller, C. M.; Gibbs, S. L.; Saez Cabezas, C. A.; Milliron, D. J. Quantitative Analysis of Extinction Coefficients of Tin-doped Indium Oxide Nanocrystal Ensembles. *Nano Lett.* **2019**, *19*, 8149–8154.
- (57) Harris, N.; Arnold, M. D.; Blaber, M. G.; Ford, M. J. Plasmonic Resonances of Closely Coupled Gold Nanosphere Chains. *J. Phys. Chem. C* **2009**, *113*, 2784–2791.
- (58) Nishijima, Y.; Rosa, L.; Juodkazis, S. Surface Plasmon Resonances in Periodic and Random Patterns of Gold Nano-disks for Broadband Light Harvesting. *Opt. Express* **2012**, *20*, 11466–11477.
- (59) Ma, Y.; Sikdar, D.; Fedosyuk, A.; Velleman, L.; Klemme, D. J.; Oh, S.-H.; Kucernak, A. R. J.; Kornyshev, A. A.; Edel, J. B. Electrotunable Nanoplasmonics for Amplified Surface Enhanced Raman Spectroscopy. *ACS Nano* **2020**, *14*, 328–336.
- (60) Yoo, S. S.; Ho, J.; Shin, D.; Kim, M.; Hong, S.; Lee, J. H.; Jeong, H. J.; Jeong, M. S.; Yi, G.; Kwon, S. J.; Yoo, P. J. Simultaneously Intensified Plasmonic and Charge Transfer Effects in Surface Enhanced Raman Scattering Sensors Using an MXene-blanketed Au Nanoparticle Assembly. J. Mater. Chem. A 2022, 10, 2945–2956.
- (61) García-Lojo, D.; Núñez-Sánchez, S.; Gómez-Graña, S.; Grzelczak, M.; Pastoriza-Santos, I.; Pérez-Juste, J.; Liz-Marzán, L. M. Plasmonic Supercrystals. Acc. Chem. Res. 2019, 52, 1855–1864.
- (62) Neubrech, F.; Huck, C.; Weber, K.; Pucci, A.; Giessen, H. Surface-Enhanced Infrared Spectroscopy Using Resonant Nanoantennas. *Chem. Rev.* **2017**, *117*, 5110–5145.
- (63) Agrawal, A.; Singh, A.; Yazdi, S.; Singh, A.; Ong, G. K.; Bustillo, K.; Johns, R. W.; Ringe, E.; Milliron, D. J. Resonant Coupling between Molecular Vibrations and Localized Surface Plasmon Resonance of Faceted Metal Oxide Nanocrystals. *Nano Lett.* **2017**, 17, 2611–2620.
- (64) Ghini, M.; Curreli, N.; Lodi, M. B.; Petrini, N.; Wang, M.; Prato, M.; Fanti, A.; Manna, L.; Kriegel, I. Control of Electronic Band Profiles Through Depletion Layer Engineering in Core—shell Nanocrystals. *Nat. Commun.* **2022**, *13*, 537.
- (65) Wang, H.; Yao, L.; Mao, X.; Wang, K.; Zhu, L.; Zhu, J. Gold Nanoparticle Superlattice Monolayer with Tunable Interparticle Gap for Surface-enhanced Raman Spectroscopy. *Nanoscale* **2019**, *11*, 13917–13923.
- (66) Green, A. M.; Ofosu, C. K.; Kang, J.; Anslyn, E. V.; Truskett, T. M.; Milliron, D. J. Assembling Inorganic Nanocrystal Gels. *Nano Lett.* **2022**, *22*, 1457–1466.
- (67) Sherman, Z. M.; Green, A. M.; Howard, M. P.; Anslyn, E. V.; Truskett, T. M.; Milliron, D. J. Colloidal Nanocrystal Gels from Thermodynamic Principles. *Acc. Chem. Res.* **2021**, *54*, 798–807.
- (68) Lounis, S. D.; Runnerstrom, E. L.; Llordés, A.; Milliron, D. J. Defect Chemistry and Plasmon Physics of Colloidal Metal Oxide Nanocrystals. *J. Phys. Chem. Lett.* **2014**, *5*, 1564–1574.
- (69) Chang, W. J.; Sakotic, Z.; Ware, A.; Green, A. M.; Roman, B. J.; Kim, K.; Truskett, T. M.; Wasserman, D.; Milliron, D. J. Wavelength Tunable Infrared Perfect Absorption in Plasmonic Nanocrystal Monolayers. ACS Nano 2024, 18, 972–982.
- (70) Vial, A.; Laroche, T. Comparison of Gold and Silver Dispersion Laws Suitable for FDTD Simulations. *Appl. Phys. B: Lasers Opt.* **2008**, 93, 139–143.

- (71) Guler, U.; Ndukaife, J. C.; Naik, G. V.; Nnanna, A. G. A.; Kildishev, A. V.; Shalaev, V. M.; Boltasseva, A. Local Heating with Lithographically Fabricated Plasmonic Titanium Nitride Nanoparticles. *Nano Lett.* **2013**, *13*, 6078–6083.
- (72) Zhu, H.; Li, Q.; Tao, C.; Hong, Y.; Xu, Z.; Shen, W.; Kaur, S.; Ghosh, P.; Qiu, M. Multispectral Camouflage for Infrared, Visible, Lasers and Microwave with Radiative Cooling. *Nat. Commun.* **2021**, *12*, 1805.
- (73) Runnerstrom, E. L.; Llordés, A.; Lounis, S. D.; Milliron, D. J. Nanostructured Electrochromic Smart Windows: Traditional Materials and NIR-selective Plasmonic Nanocrystals. *Chem. Commun.* **2014**, *50*, 10555–10572.
- (74) Lin, S.; Guan, H.; Liu, Y.; Huang, S.; Li, J.; Hasi, W.; Xu, Y.; Zou, J.; Dong, B. Binary Plasmonic Assembly Films with Hotspot-Type-Dependent Surface-Enhanced Raman Scattering Properties. ACS Appl. Mater. Interfaces 2021, 13, 53289–53299.
- (75) Prajwal, B. P.; Escobedo, F. A. Bridging Hexatic and Tetratic Phases in Binary Mixtures Through Near Critical Point Fluctuations. *Phys. Rev. Mater.* **2021**, *5*, 024003.
- (76) Cargnello, M.; Johnston-Peck, A. C.; Diroll, B. T.; Wong, E.; Datta, B.; Damodhar, D.; Doan-Nguyen, V. V. T.; Herzing, A. A.; Kagan, C. R.; Murray, C. B. Substitutional Doping in Nanocrystal Superlattices. *Nature* **2015**, *524*, 450–453.
- (77) Anderson, J. A.; Glaser, J.; Glotzer, S. C. HOOMD-blue: A Python Package for High-Performance Molecular Dynamics and Hard Particle Monte Carlo Simulations. *Comput. Mater. Sci.* **2020**, *173*, 109363
- (78) Heyes, D. M.; Melrose, J. R. Brownian Dynamics Simulations of Model Hard-Sphere Suspensions. *J. Non-Newtonian Fluid Mech.* **1993**, 46, 1–28.
- (79) Ramasubramani, V.; Dice, B. D.; Harper, E. S.; Spellings, M. P.; Anderson, J. A.; Glotzer, S. C. freud: A software suite for high throughput analysis of particle simulation data. *Comput. Phys. Commun.* **2020**, 254, 107275.
- (80) Ronneberger, O.; Fischer, P.; Brox, T. U.-N..: Convolutional Networks for Biomedical Image Segmentation. *International Conference on Medical Image Computing and Computer-Assisted Intervention* MICCAI 2015. Cham, **2015**; pp 234–241.
- (81) Pedregosa, F.; et al. Scikit-learn: Machine Learning in Python. J. Mach. Learn. Res. 2011, 12, 2825–2830.